Stellar electron-capture rates calculated with the finite-temperature relativistic random-phase approximation

Niu, Y. F.; Paar, Nils; Vretenar, Dario; Meng, Jie

Source / Izvornik: **Physical Review C - Nuclear Physics, 2011, 83**

Journal article, Published version
Rad u časopisu, Objavljena verzija rada (izdavačev PDF)

https://doi.org/10.1103/PhysRevC.83.045807

Permanent link / Trajna poveznica: https://urn.nsk.hr/urn:nbn:hr:217:940423

Stellar electron-capture rates calculated with the finite-temperature relativistic random-phase approximation

Y. F. Niu(牛一斐),[1] N. Paar,[2] D. Vretenar,[2] and J. Meng(孟杰)[3,1,4,*]

[1]*State Key Laboratory of Nuclear Physics and Technology, School of Physics, Peking University, Beijing 100871, China*

[2]*Physics Department, Faculty of Science, University of Zagreb, Zagreb, Croatia*

[3]*School of Physics and Nuclear Energy Engineering, Beihang University, Beijing 100191, China*

[4]*Department of Physics, University of Stellenbosch, Stellenbosch 7602, South Africa*

(Received 17 March 2011; published 27 April 2011)

We introduce a self-consistent microscopic theoretical framework for modeling the process of electron capture on nuclei in stellar environment, based on relativistic energy density functionals. The finite-temperature relativistic mean-field model is used to calculate the single-nucleon basis and the occupation factors in a target nucleus, and $J^\pi = 0^\pm$, $1^\pm$, and $2^\pm$ charge-exchange transitions are described by the self-consistent finite-temperature relativistic random-phase approximation. Cross sections and rates are calculated for electron capture on ^{54,56}Fe and ^{76,78}Ge in stellar environment, and results compared with predictions of similar and complementary model calculations.

DOI: 10.1103/PhysRevC.83.045807 PACS number(s): 21.60.Jz, 23.40.Bw, 23.40.Hc, 26.50.+x

I. INTRODUCTION

Weak interaction processes play a crucial role in the late evolution stages of massive stars by determining the core entropy and electron-to-baryon ratio Y_e, two important quantities associated with the dynamics of core-collapse supernovae [1]. At the end of its life, a massive star exhausts the nuclear fuel and, therefore, the core can only be stabilized by the electron degeneracy pressure as long as its mass does not exceed the corresponding Chandrasekhar mass $M_{\rm Ch}$, proportional to Y_e^2. When this mass limit is exceeded, the core cannot attain a stable configuration and it collapses. During the precollapse phase, electron capture reduces the number of electrons available for pressure support, whereas β decay acts in the opposite direction. At the same time, the neutrinos produced by electron capture freely escape from the star for values of the matter density $\lesssim 10^{11}$ g cm^{-3}, removing energy and entropy from the core [2–4]. For initial values of $Y_e \sim 0.5$, β^- decay processes can be effectively hindered by electron degeneracy, but get to be competitive when nuclei become more neutron rich.

For central stellar densities less than a few 10^{10} g/cm^3 and temperatures between 300 and 800 keV, electron capture mainly occurs on nuclei in the mass region $A \sim 60$. Under such conditions electron-capture rates are sensitive to the detailed Gamow-Teller (GT) strength distribution, because the electron chemical potential is of the same order of magnitude as the nuclear Q value (defined as the difference between neutron and proton chemical potentials). For even higher densities and temperature, nuclei with mass numbers $A > 65$ become quite abundant. The electron chemical potential is noticeably larger than the Q value, thus electron-capture rates are principally determined by the total GT strength and its centroid energy. At core densities $\rho > 10^{11}$ g/cm^3, the electron chemical potential reaches values larger than ∼20 MeV, and forbidden transitions can no longer be neglected [3,4].

Because of its relevance in modeling supernovae evolution, the process of electron capture has been studied employing various approaches, often based on available data. The first standard tabulation of nuclear weak-interaction rates for astrophysical applications was that of Fuller, Fowler, and Newman (FFN) [5–8]. It was based on the independent particle model, but used experimental information whenever available. The tables included rates for electron capture, positron capture, β decay, and positron emission for relevant nuclei in the mass range $21 \leqslant A \leqslant 60$. Shell model Monte Carlo method (SMMC) was used to determine for the first time in a fully microscopic way the GT contributions to presupernova electron-capture rates for *fp*-shell nuclei, taking into account thermal effects. The electroweak interaction matrix elements were calculated in the zero-momentum transfer limit, with the GT operators as the main ingredient. The GT strength distributions were obtained from the response function in the canonical ensemble, solved in the $0\hbar\omega$ *fp*-shell space [9]. The diagonalization of the corresponding Hamiltonian matrix in the complete *pf*-shell-model space reproduces the experimental GT$^+$ distributions [10–12]. An updated tabulation of weak interaction rates for more than 100 nuclei in the mass range $45 \leqslant A \leqslant 65$, with the same temperature and density grid as the one reported by FFN, was carried out based on the large-scale shell-model diagonalization (LSSM) approach [13].

An alternative approach to the calculation of weak-interaction rates is based on the random-phase approximation (RPA). This framework is generally more suitable for the inclusion of forbidden transitions, and for global calculations involving a large number of nuclei included in nuclear networks. To overcome the limitations of the shell model, in a study of nuclei beyond the *fp* shell a hybrid model was introduced. In this approach the SMMC is used to obtain the finite-temperature occupation numbers in the parent nucleus,

*mengj@pku.edu.cn

and the allowed and forbidden transitions for the electron-capture process are calculated in the RPA using mean-field wave functions with the SMMC occupation numbers [14]. More recently the hybrid model plus the RPA, with a global parametrization of single-particle occupation numbers, has been employed in estimates of electron-capture rates of a large number of nuclei involved in stellar core collapse [15].

Electron-capture rates were also calculated for *sd*-shell and *fpg*-shell nuclei using the proton-neutron quasiparticle RPA (QRPA) approach, based on the Nilsson model and separable GT forces [16,17]. However, the use of experimental masses for calculation of Q values limits the application of this model to nuclei with known masses. More recently a thermal QRPA approach (TQRPA) has been introduced, based on the Woods-Saxon potential and separable multipole and spin-multipole particle-hole interactions, with temperature taken into account using the thermofield dynamics (TFD) formalism [18]. A fully self-consistent microscopic framework for evaluation of nuclear weak-interaction rates at finite temperature has recently been introduced, based on Skyrme density functionals. The single-nucleon basis and the corresponding thermal occupation factors of the initial nuclear state are determined in the finite-temperature Skyrme Hartree-Fock model, and charge-exchange transitions to excited states are computed using the finite-temperature RPA [19].

An important class of nuclear structure models belongs to the framework of relativistic energy density functionals (EDFs). In particular, a number of very successful relativistic mean-field (RMF) models have been very successfully employed in analyses of a variety of nuclear structure phenomena, not only in nuclei along the valley of β stability, but also in exotic nuclei with extreme isospin values and close to the particle drip lines [20–22]. Based on this framework, the relativistic (Q)RPA (R(Q)RPA) has been developed and applied in studies of collective excitations in nuclei, including giant resonances, spin-isospin resonances, and exotic modes of excitation in unstable nuclei [23–29]. By employing a small set of universal parameters adjusted to data, both ground-state properties and collective excitations over the whole chart of nuclides, from relatively light systems to superheavy nuclei, can be accurately described. For studies of astrophysical processes, temperature effects have recently been included in the self-consistent RRPA. The low-energy monopole and dipole response of nuclei at finite temperatures were investigated [30]. An extension of the finite-temperature RRPA (FTRRPA), to include charge-exchange transitions, will certainly provide a very useful theoretical tool for studies of the electron-capture process in presupernova collapse.

In this work we introduce the theoretical framework, based on the charge-exchange FTRRPA, for the calculation of electron-capture cross sections and stellar electron-capture rates on selected medium-mass nuclei. The single nucleon basis and the thermal occupation factors of the initial nuclear state are determined in a finite-temperature RMF model, and charge-exchange transitions to the excited states are computed using the FTRRPA. The same relativistic energy density functional is consistently used both in the RMF and RPA equations. The advantage of this approach is that the calculation is completely determined by a given energy density functional and, therefore, can be extended over arbitrary mass regions of the nuclide chart, without additional assumptions or adjustment of parameters, as, for instance, single-particle energies, to transitions within specific shells. In a simple RPA, of course, correlations are described only on the one-particle–one-hole level, and therefore one cannot expect the model to reproduce the details of the fragmentation of GT strength distributions.

The paper is organized as follows. In Sec. II the framework of the charge-exchange FTRRPA and the formalism for the electron-capture cross sections and rates are introduced. The GT strength distributions at finite temperature are discussed in Sec. III. The calculated electron-capture cross sections and rates in a stellar environment are presented in Secs. IV and V, respectively. Section VI summarizes the present work and ends with an outlook for future studies.

II. FORMALISM

Since electron capture on nuclei involves charge-exchange transitions, for the purpose of the present study we extend the self-consistent FTRRPA [30] and implement the model in the charge-exchange channel. The characteristic properties of the nuclear initial state, that is, the single-nucleon basis and the corresponding thermal occupation probabilities, are obtained using a RMF model at finite temperature. This framework was introduced in Ref. [31], based on the nonlinear effective Lagrangian with the NL3 parametrization [32]. In this work the RMF at finite temperature is implemented using an effective Lagrangian with medium-dependent meson-nucleon couplings [33,34]. The corresponding FTRRPA equations are derived using the single-nucleon basis of the RMF model at finite temperature [30]. In a self-consistent approach the residual interaction terms in the FTRRPA matrix are obtained from the same Lagrangian. The proton-neutron FTRRPA equation reads

$$\begin{pmatrix} A^J_{pnp'n'} & B^J_{pnp'n'} \\ -B^J_{pnp'n'} & -A^J_{pnp'n'} \end{pmatrix} \begin{pmatrix} X^J_{p'n'} \\ Y^J_{p'n'} \end{pmatrix} = \omega_\nu \begin{pmatrix} X^J_{pn} \\ Y^J_{pn} \end{pmatrix}, \quad (1)$$

where A and B are the matrix elements of the particle-hole residual interaction,

$$A^J_{pnp'n'} = (\epsilon_P - \epsilon_H)\delta_{pp'}\delta_{nn'} + V^J_{pn'np'}(\tilde{u}_p\tilde{v}_n\tilde{u}_{p'}\tilde{v}_{n'} + \tilde{v}_p\tilde{u}_n\tilde{v}_{p'}\tilde{u}_{n'})(|f_{n'} - f_{p'}|), \quad (2)$$

$$B^J_{pnp'n'} = V^J_{pn'np'}(\tilde{u}_p\tilde{v}_n\tilde{v}_{p'}\tilde{u}_{n'} + \tilde{v}_p\tilde{u}_n\tilde{u}_{p'}\tilde{v}_{n'})(|f_{p'} - f_{n'}|). \quad (3)$$

The diagonal matrix elements contain differences of single-particle energies between particles and holes $\epsilon_P - \epsilon_H$, and these could be either $\epsilon_p - \epsilon_{\bar{n}}$ or $\epsilon_n - \epsilon_{\bar{p}}$, where p, n denote proton and neutron states, respectively. For a given proton-neutron pair configuration, the state with larger occupation probability is defined as a hole state, whereas the other one is a particle state. In the RRPA, the configuration space includes not only proton-neutron pairs in the Fermi sea, but also pairs formed from the fully or partially occupied states in the Fermi sea and the empty negative-energy states

from the Dirac sea. The residual interaction term $V^{J}_{pn'np'}$ is coupled to the angular momentum J of the final state. The spin-isospin-dependent interaction terms are generated by the exchange of π and ρ mesons. Although the direct one-pion contribution to the nuclear ground state vanishes at the mean-field level because of parity conservation, the pion nevertheless must be included in the calculation of spin-isospin excitations that contribute to the electron-capture cross section. For the ρ-meson density-dependent coupling strength we choose the same functional form used in the RMF effective interaction [34]. More details about the corresponding particle-hole residual interaction are given in Ref. [35]. The factors $f_{p(n)}$ in the matrix elements A [Eq. (2)] and B [Eq. (3)] denote the thermal occupation probabilities for protons and neutrons, respectively. These factors are given by the corresponding Fermi-Dirac distribution,

$$f_{p(n)} = \frac{1}{1+\exp\left(\frac{\epsilon_{p(n)}-\mu_{p(n)}}{kT}\right)}, \tag{4}$$

where $\mu_{p(n)}$ is the chemical potential determined by the conservation of the number of nucleons $\sum_{p(n)} f_{p(n)} = Z(N)$. The factors $\tilde{u}$, $\tilde{v}$ are introduced in order to distinguish the GT^- and GT^+ channel, that is,

$$\tilde{u}_p = 0,\ \tilde{v}_p = 1,\ \tilde{u}_n = 1,\ \tilde{v}_n = 0,\quad \text{when}\quad f_p > f_n\ \ (\bar{p}n), \tag{5}$$

$$\tilde{u}_p = 1,\ \tilde{v}_p = 0,\ \tilde{u}_n = 0,\ \tilde{v}_n = 1,\quad \text{when}\quad f_p < f_n\ \ (p\bar{n}). \tag{6}$$

With this definition the FTRRPA matrix is decoupled into two subspaces for the GT^- and GT^+ channels.

The FTRRPA equations are solved by diagonalization, and the results are the excitation energies E_ν and the corresponding forward- and backward-going amplitudes $X^{J\nu}$ and $Y^{J\nu}$, respectively. The normalization reads

$$\sum_{pn}\left[\left(X^{J\nu}_{pn}\right)^2 - \left(Y^{J\nu}_{pn}\right)^2\right](|f_p - f_n|) = 1. \tag{7}$$

The transition strengths for $GT^\pm$ operators are calculated using the relations

$$B^{T_-}_{J\nu} = \left|\sum_{pn}\left(X^{J\nu}_{pn}\tilde{u}_p\tilde{v}_n + Y^{J\nu}_{pn}\tilde{v}_p\tilde{u}_n\right)\langle p||T^-||n\rangle(|f_n - f_p|)\right|^2,$$

$$B^{T_+}_{J\nu} = \left|\sum_{pn}\left(X^{J\nu}_{pn}\tilde{v}_p\tilde{u}_n + Y^{J\nu}_{pn}\tilde{u}_p\tilde{v}_n\right)\langle p||T^+||n\rangle(|f_n - f_p|)\right|^2, \tag{8}$$

where the spin-isospin operators read $T^\pm = \sum_{i=1}^{A}\boldsymbol{\sigma}\tau_\pm$.

For the process of electron capture on a nucleus,

$$e^- + {}^{A}_{Z}X_N \rightarrow {}^{A}_{Z-1}X^*_{N+1} + \nu_e, \tag{9}$$

the cross section is derived from Fermi's golden rule,

$$\frac{d\sigma}{d\Omega} = \frac{1}{(2\pi)^2}V^2E_\nu^2\frac{1}{2}\sum_{\text{lepton spins}}\frac{1}{2J_i+1}\sum_{M_iM_f}|\langle f|\hat{H}_W|i\rangle|^2, \tag{10}$$

where V is the quantization volume, and E_ν is the energy of the outgoing electron neutrino. The weak-interaction Hamiltonian $\hat{H}_W$ of semileptonic processes is written in the current-current form [36],

$$\hat{H}_W = -\frac{G}{\sqrt{2}}\int d\boldsymbol{x}\,\mathcal{J}_\mu(\boldsymbol{x})j_\mu(\boldsymbol{x}), \tag{11}$$

where $j_\mu(\boldsymbol{x})$ and $\mathcal{J}_\mu(\boldsymbol{x})$ are the weak leptonic and hadronic current density operators, respectively. The matrix elements of leptonic part are evaluated using the standard electroweak model, and contain both vector and axial-vector components [3]. The hadronic current is obtained by using arguments of Lorentz covariance and isospin invariance of the strong interaction. The expression for the electron-capture cross sections (see Refs. [36] and [37] for more details) reads

$$\begin{aligned}\frac{d\sigma_{\text{ec}}}{d\Omega} = \frac{G_F^2\cos^2\theta_c}{2\pi}\frac{F(Z,E_e)}{(2J_i+1)}\Bigg\{&\sum_{J\geqslant 1}\mathcal{W}(E_e,E_\nu)\\ &\times\Big\{[1-(\hat{\boldsymbol{\nu}}\cdot\hat{\boldsymbol{q}})(\boldsymbol{\beta}\cdot\hat{\boldsymbol{q}})]\Big[|\langle J_f||\hat{\mathcal{T}}^{\text{mag}}_J||J_i\rangle|^2\\ &+|\langle J_f||\hat{\mathcal{T}}^{\text{el}}_J||J_i\rangle|^2\Big] - 2\hat{\boldsymbol{q}}\cdot(\hat{\boldsymbol{\nu}}-\boldsymbol{\beta})\\ &\times\text{Re}\langle J_f||\hat{\mathcal{T}}^{\text{mag}}_J||J_i\rangle\langle J_f||\hat{\mathcal{T}}^{\text{el}}_J||J_i\rangle^*\Big\}\\ &+\sum_{J\geqslant 0}\mathcal{W}(E_e,E_\nu)\{[1-\hat{\boldsymbol{\nu}}\cdot\boldsymbol{\beta}+2(\hat{\boldsymbol{\nu}}\cdot\hat{\boldsymbol{q}})(\boldsymbol{\beta}\cdot\hat{\boldsymbol{q}})]\\ &\times|\langle J_f||\hat{\mathcal{L}}_J||J_i\rangle|^2+(1+\hat{\boldsymbol{\nu}}\cdot\boldsymbol{\beta})|\langle J_f||\hat{\mathcal{M}}_J||J_i\rangle|^2\\ &-2\hat{\boldsymbol{q}}\cdot(\hat{\boldsymbol{\nu}}+\boldsymbol{\beta})\text{Re}\langle J_f||\hat{\mathcal{L}}_J||J_i\rangle\langle J_f||\hat{\mathcal{M}}_J||J_i\rangle^*\}\Bigg\},\end{aligned} \tag{12}$$

where the momentum transfer $\boldsymbol{q} = \boldsymbol{\nu} - \boldsymbol{k}$ is defined as the difference between neutrino and electron momenta, $\hat{\boldsymbol{q}}$ and $\hat{\boldsymbol{\nu}}$ are the corresponding unit vectors, and $\boldsymbol{\beta} = \boldsymbol{k}/E_e$. The energies of the incoming electron and outgoing neutrino are denoted by E_e and E_ν, respectively. The Fermi function $F(Z,E_e)$ corrects the cross section for the distortion of the electron wave function by the Coulomb field of the nucleus [38]. The explicit energy dependence of the cross section is given by the term

$$\mathcal{W}(E_e,E_\nu) = \frac{E_\nu^2}{[1+E_e/M_T(1-\hat{\boldsymbol{\nu}}\cdot\boldsymbol{\beta})]}, \tag{13}$$

where the phase-space factor $[1+E_e/M_T(1-\hat{\boldsymbol{\nu}}\cdot\boldsymbol{\beta})]^{-1}$ accounts for the nuclear recoil, and M_T is the mass of the target nucleus. The nuclear transition matrix elements between the initial state $|J_i\rangle$ and final state $|J_f\rangle$, correspond to the charge $\hat{\mathcal{M}}_J$, longitudinal $\hat{\mathcal{L}}_J$, transverse electric $\hat{\mathcal{T}}^{\text{el}}_J$, and transverse magnetic $\hat{\mathcal{T}}^{\text{mag}}_J$ multipole operators [36,37]. The initial and final nuclear states in the hadronic matrix elements are characterized by angular momentum and parity J^π. In the present calculation a number of multipoles contributing to the cross section Eq. (12) will be taken into account.

In the electron-capture process, the excitation energy of the daughter nucleus ${}^{A}_{Z-1}X_{N+1}$ is obtained by the sum of the RPA energy E_{RPA} given with respect to the ground state of the parent nucleus and the binding energy difference between daughter and parent nucleus [39]. Thus the energy of the outgoing

neutrino is determined by the conservation relation,

$$E_\nu = E_e - E_{\rm RPA} - \Delta_{np}, \tag{14}$$

where E_e is the energy of incoming electron, and $\Delta_{np} = 1.294$ MeV is the mass difference between the neutron and the proton. The axial-vector coupling constant $g_A = -1.0$ is quenched for all the multipole excitations with respect to its free-nucleon value $g_A = -1.26$. The reason to consider quenching the strength in all multipole channels, rather than just for the GT is, of course, that the axial form factor appears in all four transition operators in Eq. (12) that induce transitions between the initial and final states, irrespective of their multipolarity. The study based on the continuum RPA [40,41] showed that there is no indication of the necessity to apply any quenching to the operators responsible for the muon capture on nuclei. However, recent calculations of the muon capture rates based on the RQRPA [42], employed on a large set of nuclei, showed that reducing g_A by 10% for all multipole transitions reproduces the experimental muon capture rates to better than 10% accuracy.

The electron-capture rate is expressed in terms of the cross section Eq. (12) and the distribution of electrons $f(E_e, \mu_e, T)$ at a given temperature,

$$\lambda_{\rm ec} = \frac{1}{\pi^2\hbar^3}\int_{E_e^0}^{\infty} p_e E_e \sigma_{\rm ec}(E_e) f(E_e, \mu_e, T)\, dE_e. \tag{15}$$

$E_e^0 = \max(|Q_{if}|, m_e c^2)$ is the minimum electron energy that allows for the capture process, that is, the threshold energy for electrons, where $Q_{if} = -E_{\rm RPA} - \Delta_{np}$. $p_e = (E_e^2 - m_e^2 c^4)^{1/2}$ is the electron momentum. Under stellar conditions that correspond to the core collapse of a supernova, the electron distribution is described by the Fermi-Dirac expression [15]

$$f(E_e, \mu_e, T) = \frac{1}{\exp\left(\frac{E_e - \mu_e}{kT}\right) + 1}. \tag{16}$$

T is the temperature, and the chemical potential μ_e is determined from the baryon density ρ by inverting the relation

$$\rho Y_e = \frac{1}{\pi^2 N_A}\left(\frac{m_e c}{\hbar}\right)^3 \int_0^{\infty} (f_e - f_{e^+}) p^2\, dp, \tag{17}$$

where Y_e is the ratio of the number of electrons to the number of baryons, N_A is Avogadro's number, and f_{e^+} denotes the positron distribution function similar to Eq. (16), but with $\mu_{e^+} = -\mu_e$. We assume that the phase space is not blocked by neutrinos.

III. GAMOW-TELLER TRANSITION STRENGTH AT FINITE TEMPERATURE

In this section we present an analysis of GT transition strength distributions at finite temperature for iron isotopes and neutron-rich germanium isotopes. The GT^+ transition is the dominant process not only in electron capture on nuclei near the stability line, but also on neutron-rich nuclei because of the thermal unblocking effect at finite temperature. Here we employ the FTRRPA to calculate the GT^+ strength distribution. At zero temperature, however, pairing correlations have to be taken into account for open shell nuclei, and thus the relativistic Hartree Bogoliubov model and the QRPA with the finite-range Gogny pairing force are used in the corresponding calculations (more details are given in Ref. [27]). In atomic nuclei the phase transition from a superfluid to normal state occurs at temperatures $T \approx 0.5$–1 MeV [43–46] and, therefore, for the temperature range considered in the present analysis, the FTRRPA should provide a reasonable description of the GT transitions and electron-capture rates.

In Fig. 1 we display the GT^+ strength distributions for ^{54,56}Fe at $T = 0, 1,$ and 2 MeV, as functions of excitation energy with respect to the ground state of the parent nucleus. At zero temperature both the RQRPA and RRPA results are shown, whereas the finite-temperature transition spectra are calculated using only the FTRRPA, that is, pairing is not included in calculations at finite temperatures. The self-consistent results correspond to the DD-ME2 relativistic density functional [51]. For comparison, the GT^+ strength at zero temperature calculated with the RPA based on the Skyrme functionals SLy5 parametrization is also shown. The transition energy is higher and the strength somewhat larger as compared to the results of the relativistic model. Of course, the simple (Q)RPA approach cannot reproduce the empirical

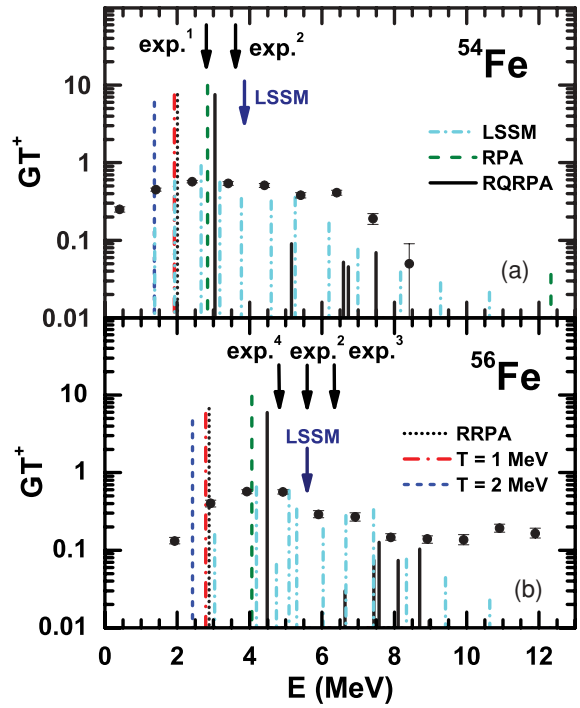

FIG. 1. (Color online) The GT^+ strength distributions for ^{54,56}Fe as functions of the excitation energy with respect to the ground state of the parent nucleus, calculated with the proton-neutron RQRPA at zero temperature, and the FTRRPA at $T = 0, 1,$ and 2 MeV, for the DD-ME2 relativistic density functional. For comparison, the GT^+ strength calculated with the nonrelativistic RPA based on the SLy5 Skyrme functional (green dashed lines), and the centroid energies (blue arrows) and distributions of the LSSM calculation [11] at $T =$ 0 MeV are shown. The experimental centroid energies from Refs. [47–50] are indicated by black arrows, and the experimental distributions from Ref. [48] for ^{54}Fe and Ref. [49] for ^{56}Fe are shown by solid circles.

fragmentation of the strength, that is, the spreading width. This could only be accomplished by including additional correlations going beyond the RPA as, for instance, in the second RPA involving $2p-2h$ configurations [52], or in the particle-vibration coupling model [39,53]. The present analysis is primarily focused on the centroid energy of GT^+ transitions, and model calculations are only carried out on the (Q)RPA level. Figure 1 also includes the centroid energies and strength distributions of a LSSM diagonalization [11]. The experimental centroid energies [47–50], defined as the energy-weighted integrated strength over the total strength, m_1/m_0, are indicated by arrows in the figure. The experimental strength distributions from Ref. [48] for ^{54}Fe and Ref. [49] for ^{56}Fe are also shown. The centroid energies and distributions obtained in the LSSM calculation and the experimental values are displayed with respect to the ground states of the parent nuclei, for convenience of comparison with the RPA results.

One might notice that the RQRPA calculation is in fair agreement with the experimental centroid energies. Compared to the LSSM, the RQRPA excitation energies are $\approx$1 MeV lower for both nuclei. By comparing the RRPA and RQRPA, we notice that pairing correlations shift the GT^+ transition to higher energy by $\sim$1–1.5 MeV, because additional energy is needed to break a proton pair. When the temperature is increased to 1 MeV, the transition energy is lowered by $\sim$1.1 MeV for ^{54}Fe, and 1.6 MeV for ^{56}Fe. This decrease in energy is mainly caused by the pairing collapse. With a further increase in temperature to 2 MeV, the GT^+ transition energy decreases by $\sim$0.5 MeV in both nuclei. This continuous decrease has its origin in the softening of the repulsive residual interaction because of the occupation factors that appear in the FTRRPA matrix elements. To demonstrate this in a quantitative way, we consider the example of ^{56}Fe, and analyze the unperturbed energies $E_{\rm unper}$, that is, the transition energy without residual interaction, and the energy shift caused by the residual interaction. For ^{56}Fe the principal contribution to the GT^+ comes from the transition from the proton orbital $\pi 1f_{7/2}$ to the neutron orbital $\nu 1f_{5/2}$. In the QRPA the unperturbed energy approximately equals the sum of two quasiparticle energies, and the chemical potential difference of neutrons and protons, resulting in $E_{\rm unper} \simeq 3.6$ MeV. The energy shift induced by the repulsive residual interaction is 0.9 MeV. If pairing correlations are not included, that is, in RPA, the unperturbed energy corresponds to the difference between the single-particle energies of the two orbitals, and this is 1.8 MeV at zero temperature, and 1.7 MeV at $T = 2$ MeV. Therefore the residual interaction shifts the energy by 1.1 MeV at zero temperature, and by 0.7 MeV at $T = 2$ MeV. Obviously the partial occupation factors (the smearing of the Fermi surface), induced either by pairing correlations or by temperature effects, will lead to the weakening of the residual interaction. The temperature effect appears to be more pronounced because the Fermi surface is more diffuse at $T = 2$ MeV. In addition to the excitation energy, the transition strength could also be reduced by the smearing of the Fermi surface through the occupation factors in Eq. (8). Therefore, the transition strength becomes weaker with increasing temperature or with the inclusion of pairing correlations. We have verified that the Ikeda sum rule [54] is satisfied at finite temperature.

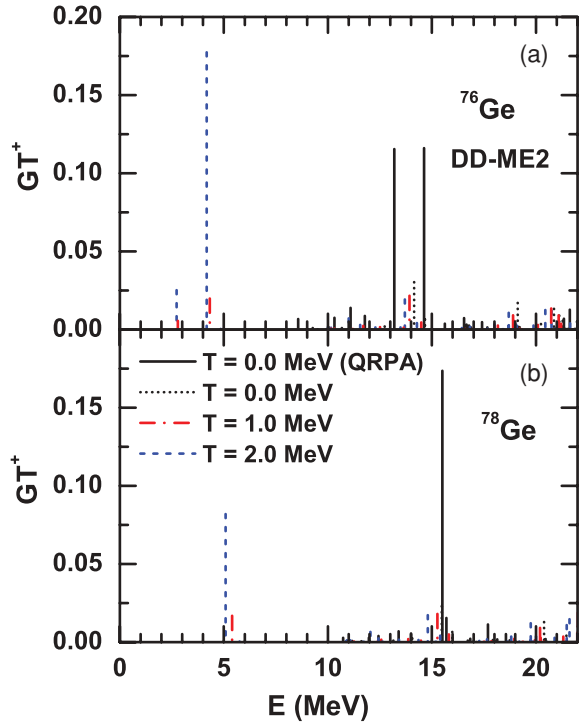

FIG. 2. (Color online) The GT^+ strength distributions of ^{76,78}Ge, calculated with the proton-neutron RQRPA at $T = 0$ MeV, and with the FTRRPA at $T = 0$, 1, and 2 MeV, using the DD-ME2 relativistic density functional.

In Fig. 2 we plot the GT^+ strength distributions of the neutron-rich nuclei ^{76,78}Ge at $T = 0$, 1, and 2 MeV. At zero temperature results obtained with both the RQRPA and the FTRRPA are shown. It is found that almost no transition strength appears at zero temperature without the inclusion of pairing correlations, because the GT^+ transition channels are Pauli blocked for these neutron-rich nuclei. As shown in the figure, the transition channels can be unblocked by two mechanisms, that is, by pairing correlations or thermal excitations. Two unblocked single-particle transitions principally contribute to the total GT^+ strength: the $\pi 1g_{9/2} \rightarrow \nu 1g_{7/2}$ particle-particle transitions, and the $\pi 1f_{7/2} \rightarrow \nu 1f_{5/2}$ hole-hole transitions, where particle (hole) denotes a state above (below) the chemical potential.

Let us consider ^{76}Ge as an example, and analyze its evolution behavior with temperature. With the inclusion of pairing correlations at $T = 0$ MeV, two major peaks are calculated at $E = 15.8$ and 16.9 MeV. The first state mainly corresponds to the transition $\pi 1f_{7/2} \rightarrow \nu 1f_{5/2}$, whereas the higher state results from a superposition of the transitions $\pi 1g_{9/2} \rightarrow \nu 1g_{7/2}$ and $\pi 1f_{5/2} \rightarrow \nu 2f_{7/2}$. At $T = 1$ MeV the GT^+ excitations shift to $E = 2.8$ and 4.3 MeV, and correspond to the transitions $\pi 1f_{7/2} \rightarrow \nu 1f_{5/2}$ and $\pi 1g_{9/2} \rightarrow \nu 1g_{7/2}$, respectively, with very weak transition strength. When the temperature is further increased to $T = 2$ MeV, the excitation energies are only slightly lowered (by 0.1 MeV), but the transition strengths are considerably enhanced.

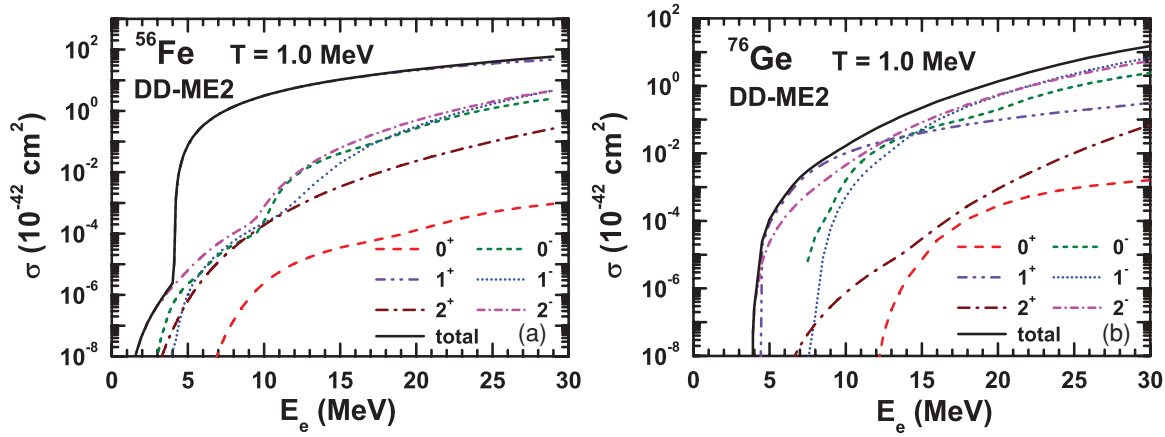

FIG. 3. (Color online) Electron-capture cross sections for the ^{56}Fe and ^{76}Ge target nuclei at $T = 1$ MeV, calculated with the FTRRPA using the DD-ME2 effective interaction. In addition to the total cross section, which includes multipole transitions $J^\pi = 0^\pm$, $1^\pm$, and $2^\pm$, contributions from the individual channels are shown in the plot as functions of the incident electron energy E_e.

The shift in energy from $T = 0$ MeV with pairing correlations, to $T = 1$ MeV is ∼13 MeV. This cannot be explained solely by the removal of the extra energy needed to break a proton pair. To explain this result, we analyze the unperturbed transition energies. It is found that the unperturbed energies are much higher when pairing correlations are included, as compared with the effect of finite temperature, resulting in considerable difference between the corresponding GT$^+$ energies. However, it is not only the pairing gaps that raise the unperturbed energy because, for instance, the pairing gaps for $\pi 1g_{9/2}$ and $\nu 1g_{7/2}$ are both ∼1.8 MeV. As these unblocked channels are particle-particle or hole-hole transitions, the sum of the quasiparticle energies $E_{\rm qp} = \sqrt{(\epsilon_p - \lambda_p)^2 + \Delta_p^2} + \sqrt{(\epsilon_n - \lambda_n)^2 + \Delta_n^2}$ is much larger than the difference of the single-particle energies $\epsilon_n - \epsilon_p$, that corresponds to the unperturbed energies at finite temperature. This decrease of GT$^+$ excitation energies is in accordance with the results of Ref. [18].

The large difference between the RQRPA GT$^+$ strength at $T = 0$ MeV and the FTRRPA strength at $T = 1$ MeV is mainly caused by the diffuseness of the Fermi surface induced by pairing correlations at zero temperature. With a further increase of temperature to $T = 2$ MeV, the Fermi surface becomes more diffuse, and this leads to enhancement of the GT$^+$ strength. A similar trend with temperature increase is found when the nucleus becomes even more neutron rich (cf. the case of ^{78}Ge in Fig. 2), but the transition channels are more difficult to unblock by thermal excitations, and this result in a weaker transition strength. In the present calculation for ^{78}Ge only the particle-particle channel $\pi 1g_{9/2} \rightarrow \nu 1g_{7/2}$ is unblocked at finite temperature.

To test the sensitivity of the results to the choice of the effective interaction, we have also carried out the same calculations for ^{54,56}Fe and ^{76,78}Ge using the relativistic density-dependent effective interaction PKDD [55]. The same general behavior is found with both interactions, but with PKDD the excitation energies are systematically larger by ∼0.5 MeV for Fe, and by 0.3 MeV for the Ge isotopes, whereas the transition strengths are slightly enhanced compared to the DD-ME2 results.

IV. ELECTRON-CAPTURE CROSS SECTIONS

In this section we calculate electron-capture cross sections for selected medium-mass target nuclei using RQRPA at zero temperature, and the FTRRPA at temperatures $T = 0$, 1, and 2 MeV. In Fig. 3 the cross sections for electron capture on ^{56}Fe and ^{76}Ge at $T = 1$ MeV are plotted as functions of the incident electron energy E_e. The cross sections are calculated using the expression of Eq. (12), and the FTRRPA with the DD-ME2 relativistic density functional [51] is used to evaluate the transition matrix elements. In addition to the total cross sections, which include multipole transitions $J^\pi = 0^\pm$, $1^\pm$, and $2^\pm$, contributions from the individual channels are shown in the plot, as functions of the incident electron energy E_e. For ^{56}Fe the total cross section is completely dominated by the 1^+ channel (GT$^+$) all the way up to $E_e = 30$ MeV, with contributions from other channels being orders of magnitude smaller. In the case of the neutron-rich nucleus ^{76}Ge, on the other hand, forbidden transitions play a more prominent role, already starting from $E_e > 12$ MeV. Their contribution to the total cross section further increases with the electron energy E_e. Obviously in systematic calculations of electron-capture rates on heavier, more neutron-rich nuclei, contributions from forbidden transitions should also be included in addition to the GT$^+$ channel.

Next we illustrate how the capture cross sections evolve with temperature. Figure 4 displays the electron-capture cross sections for the target nuclei ^{54,56}Fe at $T = 0$, 1, and 2 MeV, as functions of the incident electron energy E_e. Since for ^{54,56}Fe forbidden transitions in the range of electron energy up to 30 MeV give negligible contributions to the total cross section (cf. Fig. 3), here only the 1^+ transitions are included in the calculation. Results obtained with the proton-neutron RQRPA at $T = 0$ MeV, and with the FTRRPA at $T = 0$, 1, and 2 MeV, using the DD-ME2 effective interaction, are shown

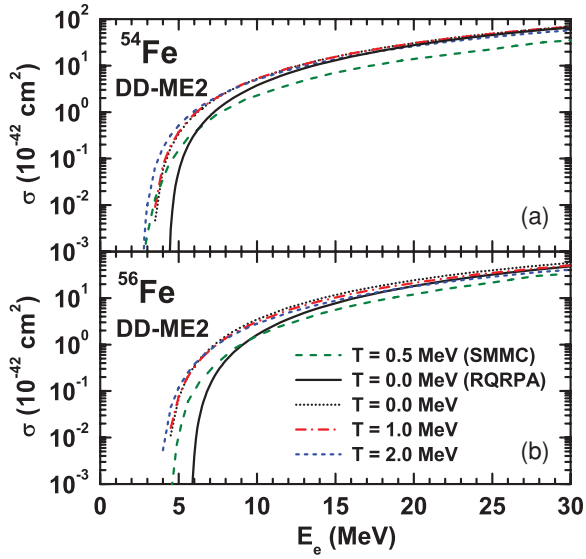

FIG. 4. (Color online) Electron-capture cross sections for the target nuclei ^{54,56}Fe at $T = 0$, 1, and 2 MeV, as functions of the incident electron energy E_e. The results obtained with the proton-neutron RQRPA at $T = 0$ MeV, and with the FTRRPA at $T = 0$, 1, and 2 MeV, using the DD-ME2 effective interaction, are shown in comparison with cross sections calculated from the SMMC GT$^+$ strength distributions [9].

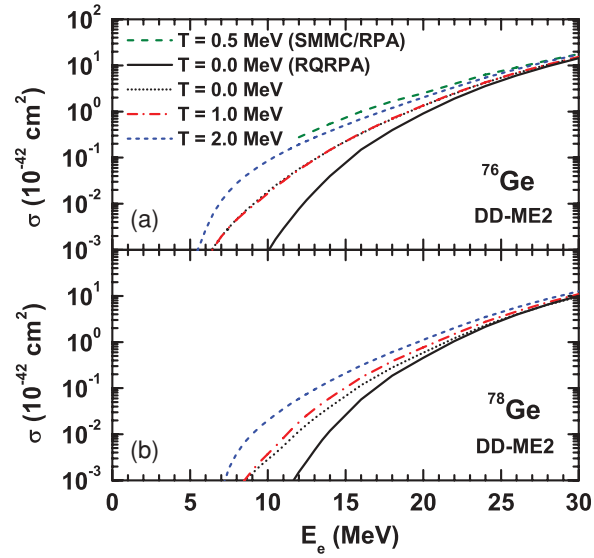

FIG. 5. (Color online) Electron-capture cross sections for the target nuclei ^{76,78}Ge at $T = 0$, 1, and 2 MeV, as functions of the incident electron energy E_e. The results are obtained by employing the DD-ME2 effective interaction in the proton-neutron RQRPA at $T = 0$ MeV, and in the FTRRPA at $T = 0$, 1, and 2 MeV. For ^{76}Ge the results are also compared with the cross section obtained in the hybrid model (SMMC-RPA) at $T = 0.5$ MeV [14].

in comparison with cross sections calculated from the SMMC GT$^+$ strength distributions [9]. Note, however, that in the SMMC calculation only the $0\hbar\omega$ GT transition strength is considered, rather than the total strength in the 1^+ channel. We notice that the principal effect of increasing the temperature in this interval is the lowering of the electron-capture threshold energy. From $T = 0$ MeV (RQRPA) to $T = 1$ MeV (FTRRPA) this decrease is more pronounced than the one from $T = 1$ to 2 MeV, in accordance with the behavior of GT$^+$ distributions discussed above. At low electron energy below 10 MeV one notices a pronounced difference between the RQRPA and FTRRPA results, reflecting the treatment of pairing correlations at zero temperature. Of course, the calculated cross sections become almost independent of temperature at high electron energies. The results of the present calculation are in qualitative agreement with those of the SMMC model [9], calculated at temperature $T = 0.5$ MeV. Cross sections calculated at very low electron energies are sensitive to the discrete level structure of the GT transitions and, therefore, one expects that the SMMC approach will produce more accurate results. These cross sections, however, are orders of magnitude smaller than those for $E_e \geqslant 10$ MeV and, when folded with the electron flux to calculate capture rates, the differences between values predicted by various models in the low-energy interval will not have a pronounced effect on the electron-capture rates.

In Fig. 5 we also illustrate the temperature dependence of the electron-capture cross sections for the neutron-rich nuclei ^{76,78}Ge. The calculation includes the multipole transitions $J^\pi = 0^\pm$, $1^\pm$, and $2^\pm$. For ^{76}Ge the results are also compared with the cross section obtained in the hybrid model (SMMC-RPA) at $T = 0.5$ MeV [14]. One might notice that the cross sections are reduced by approximately an order of magnitude when compared to the Fe isotopes, but overall a similar evolution with temperature is found. By increasing the temperature the threshold energy for electron capture is reduced. The cross sections exhibit a rather strong temperature dependence at electron energies $E_e \leqslant 12$ MeV. At $E_e = 12$ MeV, by increasing the temperature by 1 MeV, the cross sections are enhanced by approximately half an order of magnitude. Since at $E_e \leqslant 12$ MeV the electron capture predominantly corresponds to GT$^+$ transitions (see Fig. 3), the enhancement of the cross sections is caused by the thermal unblocking of the GT$^+$ channel, similar as predicted by the hybrid SMMC-RPA model [14]. For higher electron energies, forbidden transitions become more important. The results of the present analysis are in qualitative agreement with those of the TQRPA model calculation [18], and the finite-temperature RPA approach based on Skyrme functionals [19]. It is also found that the hybrid model [14] predicts slightly larger cross sections at lower energies, as anticipated due to the strong configuration mixing in SMMC calculations. In general, by increasing the number of neutrons in target nucleus, the electron capture occurs with a higher threshold and smaller cross sections.

V. STELLAR ELECTRON-CAPTURE RATES

In modeling electron-capture rates in stellar environment one assumes that the atoms are completely ionized, and the electron gas is described by the Fermi-Dirac distribution (16). By folding the FTRRPA cross sections at finite temperature with the distribution of electrons in Eq. (15), we calculate the rates for electron capture on Fe and Ge isotopes, under

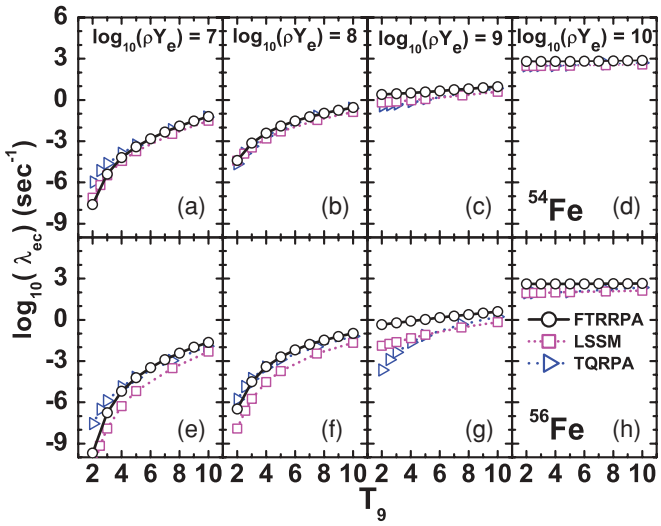

FIG. 6. (Color online) Rates for electron capture on ^{54,56}Fe as functions of the temperature T_9 ($T_9 = 10^9$ K), at selected densities ρY_e (g cm^{-3}). The results calculated using the FTRRPA with the DD-ME2 effective interaction, are shown in comparison with the rates obtained with LSSM calculations [13] and the TQRPA model [18].

different conditions associated with the initial phase of the core-collapse supernova.

Figure 6 shows the calculated rates for electron capture on ^{54,56}Fe as functions of the temperature T_9 ($T_9 = 10^9$ K) at selected densities ρY_e (g cm^{-3}). For comparison with the FTRRPA results, the rates obtained with LSSM calculations [13] and the TQRPA model [18] are also included in the figure. Here only the 1^+ transitions are included in the calculation of cross section. Although the three models compared here are based on rather different assumptions, the resulting capture rates nevertheless show similar trends. In general, the electron-capture rates increase with temperature and electron density. For high electron densities the rates increase slower, and at density $\rho Y_e = 10^{10}$ g/cm^3 the temperature dependence almost vanishes. At high densities characterized by large values of the electron chemical potential, high-energy electrons excite most or even all the GT$^+$ transitions independent of temperature. Under such conditions the increase in temperature will not have a pronounced effect on the capture rates. By increasing the number of neutrons from ^{54}Fe to ^{56}Fe, one notices that the capture rates are slightly reduced in ^{56}Fe, reflecting the behavior of the cross sections.

The FTRRPA results generally reproduce the temperature dependence of the rates predicted by the LSSM, but on the average the values calculated with the FTRRPA are somewhat larger, especially for ^{56}Fe. For ^{54}Fe and at lower densities $\rho Y_e = 10^7$ or 10^8 g/cm^3, the FTRRPA results essentially coincide with the shell-model calculation. At higher density, e.g., $\rho Y_e = 10^9$ g/cm^3, and with the electron chemical potential $\approx$5 MeV close to the threshold energy, the FTRRPA yields higher rates at lower temperature. One can understand this difference from the fragmentation of the shell-model GT$^+$ strength over the energy range 0–10 MeV [11]. While electrons at lower temperature excite all the GT$^+$ strength in FTRRPA (see Fig. 1), only a fraction of the shell-model strength is excited. Because part of the shell-model GT$^+$ strength is located at higher energies than in the FTRRPA calculation, the resulting LSSM rates are smaller. At even higher densities, e.g., at $\rho Y_e = 10^{10}$ g/cm^3 with the chemical potential $\approx$11 MeV, already at lower temperatures the high-energy electrons excite all the transition shell-model strength, and the resulting rates are essentially the same as those calculated with the FTRRPA. For electron capture on ^{56}Fe, at lower densities $\rho Y_e = 10^7$ and 10^8 g/cm^3 the FTRRPA results are in better agreement with the TQRPA calculation, whereas the LSSM predicts lower rates. At higher densities the trend predicted by the FTRRPA is closer to the LSSM, but the calculated values are still above the shell-model results. In general, the differences between the FTRRPA and the shell-model rates are larger in ^{56}Fe than ^{54}Fe. The principal reason lies in the difference between the GT$^+$ centroid energies calculated in the two models (cf. see Fig. 1). As in the case of ^{54}Fe, the largest difference between the FTRRPA and LSSM is at $\rho Y_e = 10^9$ g/cm^3, because the electron chemical potential at this density is close to the threshold energy, hence the capture rates are sensitive to the detailed GT$^+$ distribution.

Figure 7 compares the rates for electron capture on ^{76,78}Ge, calculated using the FTRRPA with the DD-ME2 effective interaction, to the values obtained with the hybrid model (SMMC-RPA) and the TQRPA model [18]. In order to allow a direct comparison with the hybrid model, the same quenching of the axial-vector coupling constant with respect to its free-nucleon value is employed, i.e., $g_A^* = 0.7 g_A$. Because for ^{76,78}Ge the contribution of forbidden transition is not negligible, the calculations of rates Eq. (12) includes the multipole transitions $J^\pi = 0^\pm$, $1^\pm$, and $2^\pm$. Similar to the case of Fe nuclei, the calculated capture rates increase with temperature and density, and are reduced by adding neutrons from ^{76}Ge to ^{78}Ge. For ^{76,78}Ge the rates predicted by the FTRRPA display a temperature and density dependence very similar to that of the

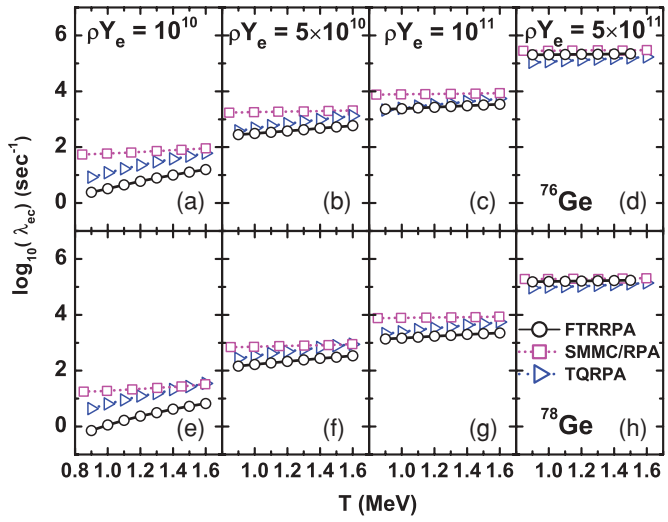

FIG. 7. (Color online) Rates for electron capture on ^{76,78}Ge as functions of the temperature, at selected densities ρY_e (g cm^{-3}). The results calculated using the FTRRPA with the DD-ME2 effective interaction, are shown in comparison with the rates obtained with the hybrid model (SMMC-RPA) and the TQRPA model [18].

TQRPA model, whereas the hybrid model predicts a very weak temperature dependence at all densities considered in Fig. 7. In general, both the FTRRPA and the TQRPA predict smaller values of capture rates compared to the hybrid model. The reason is that the probability of unblocking transition channels is larger in the hybrid model because it includes many-body correlations beyond the RPA level. At the density $\rho Y_e = 10^{10}$ g/cm^3 the FTRRPA capture rates exhibit a relatively strong temperature dependence. The electron chemical potential is ≈11 MeV, and the cross sections are dominated by GT$^+$ transitions. By increasing temperature the GT$^+$ transitions are unblocked, resulting in a large enhancement of the cross sections as shown in Fig. 5. A similar trend is also predicted by the TQRPA calculation [18], whereas the temperature dependence of the capture rates is much weaker in the hybrid model. With a further increase in density to $\rho Y_e = 10^{11}$ g/cm^3, the chemical potential reaches ≈23 MeV. At these energies forbidden transitions dominate the calculated cross sections, the FTRRPA yields cross sections similar to the TQRPA, and the same for the capture rates. At even higher densities the temperature dependence of the FTRRPA and TQRPA results becomes weaker, because the cross sections are less sensitive to temperature. At the density $\rho Y_e = 5 \times 10^{11}$ g/cm^3 the capture rates predicted by the FTRRPA are larger than the TQRPA results, and reach values similar to those of the hybrid model.

VI. CONCLUSION

In this work we have introduced a self-consistent theoretical framework for modeling the process of electron capture in the initial phase of supernova core collapse, based on relativistic energy density functionals. The finite-temperature RMF model is employed to determine the single particle energies, wave functions, and thermal occupation probabilities for the initial nuclear states. The relevant charge-exchange transitions $J^\pi = 0^\pm$, $1^\pm$, and $2^\pm$ are described by the FTRRPA. The FTRMF+FTRRPA framework is self-consistent in the sense that the same relativistic energy density functional is employed both in the finite-temperature RMF model and in the RRPA matrix equations.

In the calculation of the electron-capture cross sections, the GT$^+$ transitions provide the major contribution in the case of ^{54,56}Fe, whereas for more neutron-rich nuclei such as ^{76,78}Ge forbidden transitions play a more prominent role already starting at incident electron energy above ≈10 MeV. The principal effect of increasing temperature is the lowering of the electron-capture threshold energy. For ^{76,78}Ge the cross sections in the low-energy region are sensitive to temperature because of the dominant role of GT$^+$ transition channel, but these correlation becomes weaker at higher energies dominated by major contributions from forbidden transitions.

Electron-capture rates for different stellar environments, densities, and temperatures, characteristic for core collapse supernovae, have been calculated and compared with previous results of shell-model, hybrid shell-model plus RPA, and TQRPA calculations. For ^{54,56}Fe, the FTRRPA results generally reproduce the temperature dependence of the rates predicted by shell-model calculations, but on the average the values calculated with the FTRRPA are somewhat larger, especially for ^{56}Fe. For ^{76,78}Ge the FTRRPA capture rates display a trend very similar to that of the TQRPA calculation, especially for the temperature dependence, whereas this dependence of the capture rates is much weaker in the hybrid model.

The results obtained in the present study demonstrate that the framework of finite-temperature RMF and FTRRPA provides a universal theoretical tool for the analysis of stellar weak-interaction processes in a fully consistent microscopic approach. This is especially important for regions of neutron-rich nuclei where the shell-model diagonalization approach is not feasible. A microscopic approach has a big advantage in comparison to empirical models that explicitly necessitate data as input for calculations, as in many mass regions data will not be available. Of course, the present framework is limited to the level of RPA and does not include important many-body correlations that are taken into account in a shell-model approach. However, as discussed previously, at higher densities and temperatures in the stellar environment, the detailed fragmentation of transition spectra does not play such a significant role, and the FTRRPA represents a very good approximate framework that can be used in systematic calculations of electron-capture rates. Further improvements of the current version of the model are under development. For open-shell nuclei at very low temperatures, pairing correlations need to be taken into account. To obtain the empirical fragmentation of the transition spectra, the inclusion of higher-order correlations beyond the RPA level, that is, the coupling to $2p - 2h$ states will be necessary.

ACKNOWLEDGMENTS

Y.F.N. would like to acknowledge discussions with Z. M. Niu and H. Z. Liang. This work is supported by the State 973 Program 2007CB815000, the NSF of China under Grants No. 10975007 and No. 10975008, the Unity through Knowledge Fund (UKF Grant No. 17/08), and by MZOS project 1191005-1010, and the Chinese-Croatian project "Nuclear structure and astrophysical applications."

[1] H. A. Bethe, G. E. Brown, J. Applegate, and J. M. Lattimer, Nucl. Phys. A **324**, 487 (1979).
[2] H. A. Bethe, Rev. Mod. Phys. **62**, 801 (1990).
[3] K. Langanke and G. Martínez-Pinedo, Rev. Mod. Phys. **75**, 819 (2003).
[4] H.-T. Janka, K. Langanke, A. Marek, G. Martínez-Pinedo, and B. Müller, Phys. Rep. **442**, 38 (2007).
[5] G. M. Fuller, W. A. Fowler, and M. J. Newman, Astrophys. J. Suppl. Ser. **42**, 447 (1980).

[6] G. M. Fuller, W. A. Fowler, and M. J. Newman, Astrophys. J. Suppl. Ser. **48**, 279 (1982).
[7] G. M. Fuller, W. A. Fowler, and M. J. Newman, Astrophys. J. **252**, 715 (1982).
[8] G. M. Fuller, W. A. Fowler, and M. J. Newman, Astrophys. J. **293**, 1 (1985).
[9] D. J. Dean, K. Langanke, L. Chatterjee, P. B. Radha, and M. R. Strayer, Phys. Rev. C **58**, 536 (1998).
[10] K. Langanke and G. Martínez-Pinedo, Phys. Lett. B **436**, 19 (1998).
[11] E. Caurier, K. Langanke, G. Martínez-Pinedo, and F. Nowacki, Nucl. Phys. A **653**, 439 (1999).
[12] K. Langanke and G. Martínez-Pinedo, Nucl. Phys. A **673**, 481 (2000).
[13] K. Langanke and G. Martínez-Pinedo, At. Data Nucl. Data Tables **79**, 1 (2001).
[14] K. Langanke, E. Kolbe, and D. J. Dean, Phys. Rev. C **63**, 032801 (2001).
[15] A. Juodagalvis, K. Langanke, W. R. Hix, G. Martínez-Pinedo, and J. M. Sampaio, Nucl. Phys. A **848**, 454 (2010).
[16] J.-U. Nabi and H. V. Klapdor-Kleingrothaus, At. Data Nucl. Data Tables **71**, 149 (1999).
[17] J.-U. Nabi and H. V. Klapdor-Kleingrothaus, At. Data Nucl. Data Tables **88**, 237 (2004).
[18] A. A. Dzhioev, A. I. Vdovin, V. Y. Ponomarev, J. Wambach, K. Langanke, and G. Martínez-Pinedo, Phys. Rev. C **81**, 015804 (2010).
[19] N. Paar, G. Colò, E. Khan, and D. Vretenar, Phys. Rev. C **80**, 055801 (2009).
[20] P. Ring, Prog. Part. Nucl. Phys. **37**, 193 (1996).
[21] J. Meng, H. Toki, S. Zhou, S. Zhang, W. Long, and L. Geng, Prog. Part. Nucl. Phys. **57**, 470 (2006).
[22] D. Vretenar, A. V. Afanasjev, G. A. Lalazissis, and P. Ring, Phys. Rep. **409**, 101 (2005).
[23] Z. Ma, N. Van Giai, A. Wandelt, D. Vretenar, and P. Ring, Nucl. Phys. A **686**, 173 (2001).
[24] P. Ring, Z. Ma, N. Van Giai, D. Vretenar, A. Wandelt, and L. Cao, Nucl. Phys. A **694**, 249 (2001).
[25] T. Nikšić, D. Vretenar, and P. Ring, Phys. Rev. C **66**, 064302 (2002).
[26] N. Paar, P. Ring, T. Nikšić, and D. Vretenar, Phys. Rev. C **67**, 034312 (2003).
[27] N. Paar, T. Nikšić, D. Vretenar, and P. Ring, Phys. Rev. C **69**, 054303 (2004).
[28] H. Liang, N. Van Giai, and J. Meng, Phys. Rev. Lett. **101**, 122502 (2008).
[29] N. Paar, D. Vretenar, E. Khan, and G. Colò, Rep. Prog. Phys. **70**, 691 (2007).
[30] Y. F. Niu, N. Paar, D. Vretenar, and J. Meng, Phys. Lett. B **681**, 315 (2009).
[31] Y. K. Gambhir, J. P. Maharana, G. A. Lalazissis, C. P. Panos, and P. Ring, Phys. Rev. C **62**, 054610 (2000).
[32] G. A. Lalazissis, J. König, and P. Ring, Phys. Rev. C **55**, 540 (1997).
[33] S. Typel and H. H. Wolter, Nucl. Phys. A **656**, 331 (1999).
[34] T. Nikšić, D. Vretenar, P. Finelli, and P. Ring, Phys. Rev. C **66**, 024306 (2002).
[35] N. Paar, T. Nikšić, D. Vretenar, and P. Ring, Phys. Rev. C **69**, 054303 (2004).
[36] J. D. Walecka, *Muon Physics* (Academic, New York, 1975), Vol. II.
[37] J. S. O'Connell, T. W. Donnelly, and J. D. Walecka, Phys. Rev. C **6**, 719 (1972).
[38] E. Kolbe, K. Langanke, G. Martínez-Pinedo, and P. Vogel, J. Phys. G **29**, 2569 (2003).
[39] G. Colò, N. Van Giai, P. F. Bortignon, and R. A. Broglia, Phys. Rev. C **50**, 1496 (1994).
[40] E. Kolbe, K. Langanke, and P. Vogel, Phys. Rev. C **50**, 2576 (1994).
[41] E. Kolbe, K. Langanke, and P. Vogel, Phys. Rev. C **62**, 055502 (2000).
[42] T. Marketin, N. Paar, T. Nikšić, and D. Vretenar, Phys. Rev. C **79**, 054323 (2009).
[43] E. Khan, N. Van Giai, and N. Sandulescu, Nucl. Phys. A **789**, 94 (2007).
[44] A. L. Goodman, Nucl. Phys. A **352**, 30 (1981).
[45] A. L. Goodman, Nucl. Phys. A **352**, 45 (1981).
[46] J. Cooperstein and J. Wambach, Nucl. Phys. A **420**, 591 (1984).
[47] M. C. Vetterli *et al.*, Phys. Rev. C **40**, 559 (1989).
[48] T. Rönnqvist *et al.*, Nucl. Phys. A **563**, 225 (1993).
[49] S. El-Kateb *et al.*, Phys. Rev. C **49**, 3128 (1994).
[50] D. Frekers, Nucl. Phys. A **752**, 580 (2005).
[51] G. A. Lalazissis, T. Nikšić, D. Vretenar, and P. Ring, Phys. Rev. C **71**, 024312 (2005).
[52] S. Drożdż, S. Nishizaki, J. Speth, and J. Wambach, Phys. Rep. **197**, 1 (1990).
[53] E. Litvinova, P. Ring, and D. Vretenar, Phys. Lett. B **647**, 111 (2007).
[54] K. Ikeda, S. Fujii, and J. I. Fujita, Phys. Lett. **3**, 271 (1963).
[55] W. Long, J. Meng, N. Van Giai, and S.-G. Zhou, Phys. Rev. C **69**, 034319 (2004).